J. Fluid Mech. (1996), *vol.* 322, *pp.* 383–409

Experiments on density-gradient anisotropies and scalar dissipation of turbulence in a stably stratified fluid

By S. T. THORODDSEN[1] AND C. W. VAN ATTA[2]†

[1] Department of Theoretical and Applied Mechanics, University of Illinois at Urbana-Champaign, Urbana IL 61801-2935, USA

[2]Applied Mechanics and Engineering Sciences, University of California, San Diego, La Jolla, CA 92093-0411, USA

(Received 23 February 1995 and in revised form 27 April 1996)

The anisotropic behaviour of density-gradient fluctuations in stably stratified grid turbulence and the consequences for simplified (isotropic) estimates of scalar dissipation rates χ were experimentally studied in a thermally stratified wind tunnel at moderate Reynolds numbers ($Re_\lambda \simeq 20$). Strong stable stratifications were attained, with Brunt–Väisälä frequency N as high as 4 rad s^{-1}. The correlation method was used to estimate the mean-square cross-stream and streamwise density gradients. Cross-stream gradients were measured using two cold wires. The mean-square vertical gradients were found to become larger than the streamwise gradients by as much as a factor of 2.2 for the largest dimensionless buoyancy times ($Nt = 7$). This corresponds to a 40% error in the scalar dissipation estimates based on $\partial\theta/\partial x$ alone, and assuming the validity of the isotropic relations. Gradient spectral relations show that this buoyancy-induced anisotropy persists at all length scales. Better closure of the scalar variance balance was attained than in previously reported measurements by other researchers. This is attributed to our use of cold-wire temperature sensors having larger length-to-diameter ratio than used in the previous measurements.

1. Introduction

Turbulent stirring and mixing of scalars is an ubiquitous process in geophysical flows. The mixing scalar (e.g. temperature, salinity) often introduces density stratifications and therefore has a direct influence on the dynamics of the turbulent stirring process through buoyancy forces. In geophysical flows the magnitude of mixing or dissipation of scalar fluctuations are usually deduced from unidirectional measurements of scalar gradients, e.g. by vertical dropsondes in the ocean and horizontal tracks in the atmosphere. It is therefore important to know how accurate these approximations, invariably based on isotropic relations, are under conditions of strong stable stratification. Thoroddsen & Van Atta (1989, 1992*a*) have shown that in stably stratified grid turbulence the stratification induces strong anisotropies in the vertical *vs.* streamwise strain rates, i.e. the ratio of the mean-square values of $\partial w/\partial x$ and $\partial u/\partial x$ strongly departs from the isotropic value for low turbulent Froude numbers. The experiments described here were conducted to investigate whether

† Also Scripps Institution of Oceanography.

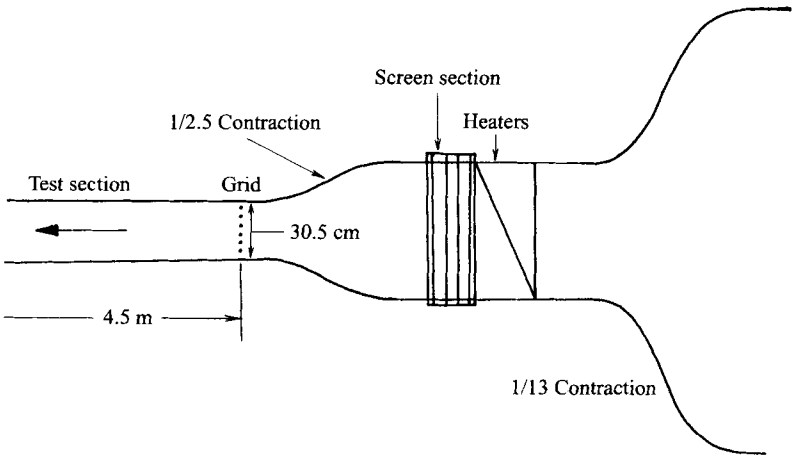

FIGURE 1. Schematic of the thermally stratified wind tunnel.

similar anisotropies also exist in the density gradients and how these might influence simplified estimates of the scalar dissipation rate χ. Measurements in non-stratified flows by Browne, Antonia & Shah (1987) and Krishnamoorthy & Antonia (1987) have shown that scalar-gradient anisotropies exist in a heated turbulent wake and in a passively heated turbulent boundary layer, respectively. The above-mentioned flows are highly inhomogeneous, possessing large-scale mean strain. The generation mechanism of the grid turbulence studied here is however close to spatially homogeneous, resulting, in the non-stratified case, in a nearly isotropic turbulence only a few mesh lengths downstream from the grid. Grid turbulence has therefore been used as the prototypical example of turbulent fields close to isotropy and is thus ideal for identifying the source and development of anisotropies due to buoyancy forces, since it is not affected by the large-scale non-homogeneities present in wakes, jets and boundary layers.

For the quasi-two-dimensional turbulence state observed at much larger buoyancy times than studied here, very large velocity-gradient anisotropies have been observed by Yap & Van Atta (1993) and Fincham, Maxworthy & Spedding (1994).

Studies of isotropic scalar fields, without density stratifications, generated by heated grids, have been done by Mills *et al.* (1958), Yeh & Van Atta (1973) and Warhaft & Lumley (1978) to name a few. Warhaft & Lumley studied temperature fluctuations where the velocity fluctuations were generated by a biplanar grid, but a separate fine zither was used to produce the temperature fluctuations, thus reaching a better understanding of the importance of the relative turbulent scale size of the velocity and scalar fields.

2. Experimental setup

2.1. *Thermally stratified wind tunnel*

The experiments were conducted in a thermally stratified wind tunnel, shown in figure 1. The evolution of stably stratified grid-generated turbulence was previously studied in this same experimental facility by Lienhard & Van Atta (1990). The thermal stratification was produced by an electric heater consisting of heater rods and numerous metal triangular fins aligned vertically in the streamwise direction.

The 45 heater rods passed through the plates and were wired in 16 independent electrically controllable sets. Additional unheated triangular plates were included to counterbalance the fin drag and maintain uniform mean velocity in the test section. The design specifications of the heating setup are given in Lienhard & Van Atta (1989). The wind tunnel was slightly modified before the present experiments. An extra screen section was added to dampen velocity and temperature fluctuations generated by the heaters. This screen section was located after the heater upstream of the contraction and had four steel screens with mesh size of about 1 mm. The r.m.s. temperature and velocity fluctuations after the screen section were reduced by a factor of 3 from previous results without screens.

The turbulence was generated by a biplanar grid of 0.48 cm diameter circular steel cylinders with a mesh size M of 2.54 cm. The resulting solidity of the grid was 31%.

The turbulent and mean-value Reynolds numbers are here defined as

$$Re_\lambda = \frac{u'\lambda}{\nu}, \quad Re_\ell = \frac{u'\ell}{\nu}, \quad Re_M = \frac{UM}{\nu}. \tag{2.1}$$

Their values close to the grids, but after initial transients, are approximately 20, 50 and 3200 respectively. Here λ is the Taylor microscale and the value of the overturning length scale ℓ was evaluated from the dissipation as $(u')^3/\epsilon$.

The temperature gradient measurements were taken for four different stratification strengths, giving a Brunt–Väisälä frequency $N = [(g/T_0)(\mathrm{d}T/\mathrm{d}z)]^{1/2}$ of 1.25, 2.53, 3.06 and 4.03 rad s^{-1}, where g is the gravitational acceleration, $T(z)$ is the mean temperature, and z is the vertical coordinate. The strongest stratification could be achieved only in a thin layer, about 7.5 cm in depth, in the centre of the tunnel. It is important to achieve a linear temperature gradient in the test section to assure cross-sectional homogeneity of the temperature fluctuations θ since the scalar fluctuations are due to the grid-induced vertical movement of fluid elements relative to this background mean density gradient. Figure 2 shows the mean temperature profiles for various stratification strengths. The close linearity of these profiles, on the tunnel centreline, is evident from this figure. Table 1 lists the mean temperature gradients and the corresponding mean velocities during the experimental runs. Mean vertical temperature gradient measurements at different down-stream locations in the tunnel showed that N was independent of streamwise location.

The coordinate system used in the subsequent sections locates the origin at the grid with the x-axis pointing downstream and the z-axis upwards in the vertical direction.

2.2. *Instrumentation*

2.2.1. *Velocity and buoyancy flux measurements*

The measurements described in this paper focus on the statistics of temperature, but some measurements were also made of fluctuating velocities to identify the dynamical states of the turbulence. The vertical and horizontal fluctuating velocities were measured using an $\times$-wire probe, thermally corrected by two cold wires placed one on each side of the hot wires. The mean instantaneous temperature measured by the two cold wires was used to correct the hot-wire signals for the effect of flow temperature, since the hot wires respond to both the velocity and temperature of the flow. Extensive calibrations of the $\times$-wire/cold-wires probe were performed before and after each experimental run. This calibration included yaw-angle calibration as well as velocity calibrations at many different constant levels of flow mean temperature. Calibration coefficients including corrections for the temperature effects were estimated from these calibration data according to the formula derived by Lienhard & Van Atta (1990,

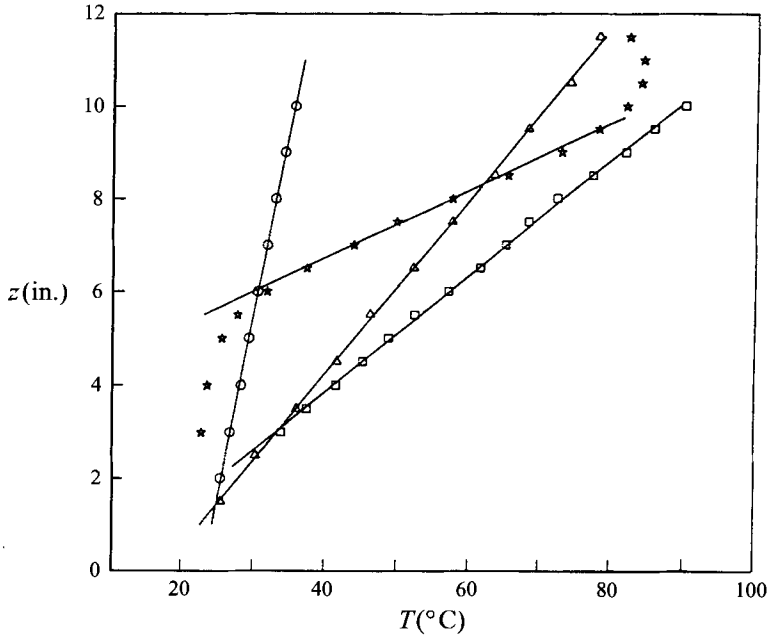

FIGURE 2. Mean vertical profiles of temperature, for the four different stratification strengths N: 1.25 (rad s^{-1}) (○); 2.53 (△); 3.06 (□) and 4.03 (*).

N(rad s^{-1})	dT/dz (°C m^{-1})	U(m s^{-1})
1.25	48.4	2.17
2.53	210.0	2.12
3.06	315.0	1.81
4.03	542.0	2.18

TABLE 1. Mean vertical temperature gradient and mean streamwise velocity for the different stratification strengths

p. 62). The subsequent measurements of turbulent velocities were performed for the same tunnel setups used for the corresponding temperature gradient measurements. We used a Dantec 55P61 ×-wire probe and two cold wires positioned within 1 mm on both sides of the ×-wire as shown in figure 3(*a*).

Velocity measurements were not conducted for the strongest of the stratifications (N=4 rad s^{-1}) due to the very large temperature fluctuations in the flow which would have contaminated the velocity signals excessively.

2.2.2. *Measurements of fluctuating temperature*

Instantaneous temperature measurements were made with cold wires, fabricated in the laboratory. The wire material was platinum, etched from Wollaston wire (0.65 μm dia.) and silver-soldered under a microscope to Dantec 55P11 single hot-wire prongs. The prongs were pre-bent to obtain the desired wire lengths. Care was taken to make the wires as straight as possible. The prong tips were first filed down to a sharp point, then small drops of silver solder were placed at the tips and a small film of viscous flux placed on top of the solder. Very viscous flux was needed for the film to wet the

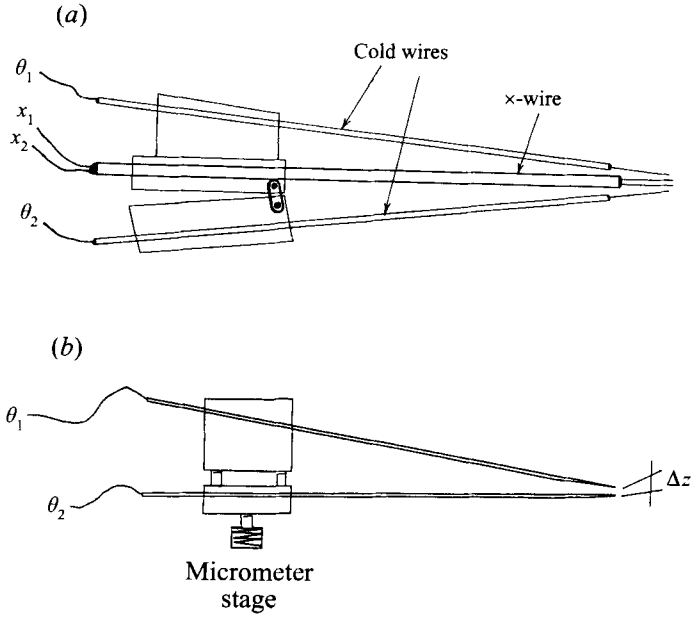

FIGURE 3. The arrangement of the experimental probes. (*a*) Top-view of the x-wire/2-cold-wire probe used for u, w and θ measurements. (*b*) Two-cold-wire probe for measuring $\partial\theta/\partial z$. The two transducers are mounted on opposite sides of a micrometer stage, allowing for fine adjustment of their separation.

tip of the sharpened prongs and not be dragged, by the surface tension, into a drop under the tip. This flux would attract the platinum wire to the solder and touching the prong with the soldering iron fused the connection. The second connection had to be made with the wire having a small arc in it since the second connection tended to stretch the wire and, without the arc, break it.

The cold-wire d.c.-circuits were also made in-house and the basic design is described in Haugdahl & Lienhard (1988). The cold-wire current used was 200 μA.

Selecting the right cold-wire length is not trivial. There is a trade-off between attaining sufficient spatial resolution and retaining an adequate frequency response of the instrument. There is a need for as short a wire as possible to get good spatial resolution, but prong effects have been shown to affect the signal if the ratio of wire length to diameter is not large enough, e.g. Browne & Antonia (1987). These measurements showed that to avoid serious attenuation of the measured temperature fluctuations one needs at least $L_w/D_w > 1000$. There is also a practical lower limit for the diameter of the wire, due to fragility and difficulty in fabrication. We have used 0.65 μm wire diameter and approximately 0.7 mm wire length. The improved closure of the scalar variance balance achieved here indicates that this wire size succeeded in resolving all of the significant scales of the temperature fluctuations.

The Prandtl number $Pr = \nu/\alpha$ is the ratio of the kinematic viscosity and the thermal diffusivity and has the value of 0.71 for temperature in air. The smallest turbulent temperature scales are thereby characterized by the Batchelor scale η_θ (Batchelor 1959),

$$\eta_\theta = \left(\frac{\nu\alpha^2}{\epsilon}\right)^{1/4} = \eta\ Pr^{-1/2} \tag{2.2}$$

where η is the Kolmogorov microscale

$$\eta = \left(\frac{\nu^3}{\epsilon}\right)^{1/4}, \tag{2.3}$$

and ϵ is the viscous dissipation of turbulent kinetic energy. The smallest values of η_θ were observed close to the turbulence-generating grids and were about 0.3 mm, growing downstream as the turbulence decays, becoming larger than 1 mm farthest downstream.

2.2.3. *Measurements of the spatial correlation of temperature*

Single-wire measurements of temperature coupled with the application of Taylors' hypothesis were used to estimate the streamwise correlation of temperature.

However, to estimate the cross-stream correlation of temperature in the turbulent field, two cold wires were used. The separation of these two wires was adjusted by a small micrometer stage. Figure 3(*b*) shows schematically the micrometer-connected probe holders. The initial separation of the cold wires was determined before the probes were moved into the tunnel by using a cathetometer on a stand sitting next to the wind tunnel. The separation of the wires was measured with the cathetometer for a few different adjusted separations on the micrometer. The initial separation could thus be deduced from the off-set in cathetometer readings due to a known change in the micrometer setting. The two wires could be brought as close as 0.2 mm with an accuracy of 0.02 mm. The wire spans were straight only to that precision, so more accurate initial positioning was not neccessary or meaningful. The probe holders with the wires were then moved into the tunnel. Once in the tunnel the separation of the wires was varied using a lever that was connected through two universal joints from the micrometer knob out through a slot in the tunnel floor. The traversing mechanism was supported on a rail under the tunnel and the airfoil-shaped wing holding the probes travelled along a horizontal slot in the floor. This slot was incrementally closed with wedged-in segments and sealed with duct-tape.

The micrometer setup was tested for possible thermal expansion due to the much hotter air inside the tunnel during the stratified runs. This was done by using a cathetometer positioned just outside the tunnel to measure the separation of the cold wires *in situ* in the tunnel before and after the flow in the tunnel was heated. The thermal expansion of the setup was smaller than the experimental error in reading the wire separations and was thus neglected. The initial separation of the cold wires was thus, in subsequent runs, measured outside the tunnel using the cathetometer.

The mean velocity during the correlation studies was measured with a Pitot tube placed right next to the cold wires, accounting for the temperature dependence of the mean fluid density at the vertical location of the Pitot-tube in the flow.

2.3. *The correlation method*

Temperature gradients can in theory be estimated by the finite difference in temperature measured simultaneously by two closely spaced cold wires, but for a very close spacing of the two wires the inaccuracies in their individual calibrations will overwhelm the gradient signal. To overcome this difficulty the so-called *correlation method* was used to obtain the mean-square spatial gradients of temperature. This method is based on the parabolic behaviour of the temperature correlation function for small separations of two measurement points A and B. This method avoids the errors associated with inaccuracies in the calibrations of the two cold wires. The correlation coefficient can be calculated from the linear cold-wire voltages without performing a

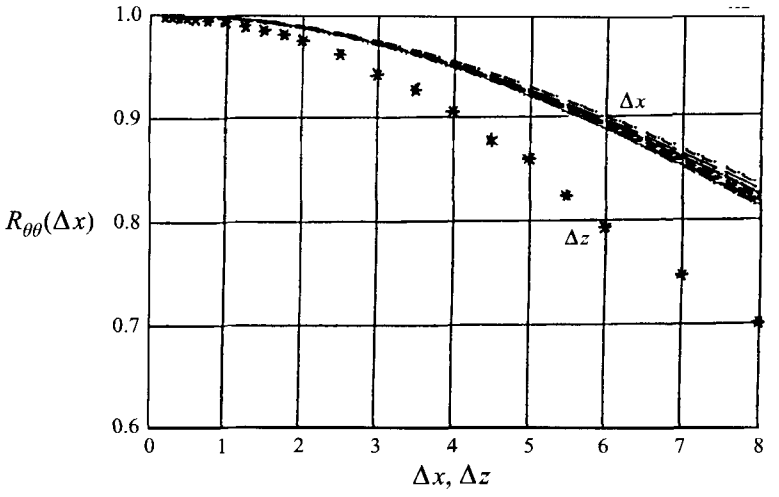

FIGURE 4. Typical auto- and cross-correlations of the temperature fluctuations, versus change in Δx (lines) and Δz (*).

calibration, since when calculating correlation coefficients one subtracts the mean and normalizes by the r.m.s. values anyway. The correlation coefficient therefore depends only on the frequency response of the wires and not on any systematic calibration offset.

The cross-correlation coefficient of the temperature at two points A and B separated by Δx is defined as

$$(R_{\theta\theta})_{A,B}(\Delta x) = \frac{\overline{\theta(x)\theta(x+\Delta x)}}{\theta'_A \theta'_B}.$$

With the assumed homogeneity of the turbulent scalar field, this cross-correlation is an even function of the separation Δx. The cross-correlation can therefore be expanded in a Taylor series about zero separation, following the notation of Krishnamoorthy & Antonia (1987):

$$R_{\theta\theta}(\Delta x) = 1 - \frac{(\Delta x)^2}{2\lambda^2} + O(\Delta x)^4 \tag{2.4}$$

where the Taylor microscale λ for temperature is defined as follows†:

$$\lambda^2 = \overline{\theta^2}/\overline{(\partial\theta/\partial x)^2}.$$

If one plots on a log-log graph the quantity $1-R(\Delta x)$ *vs.* Δx the measurements should fall on a line with slope 2 if they follow relation (2.4). The vertical location of this best-fit line indicates the relative mean-square magnitude of the r.m.s. temperature and the r.m.s. temperature gradient. By performing this procedure in Δx and Δz we can estimate the ratio of the mean-square gradients in those two directions.

Figure 4 shows the shape of typical temperature correlation curves for separations in the streamwise x- and vertical z-directions. The streamwise correlations were calculated for every Δz separation, thus giving the number of different lines shown in the figure.

The spatial resolution of the cold wires becomes especially important for very small

† Some authors use a definition of the temperature Taylor scale larger by a factor of $\sqrt{2}$, but we have followed the same definition as used for the Taylor velocity scale.

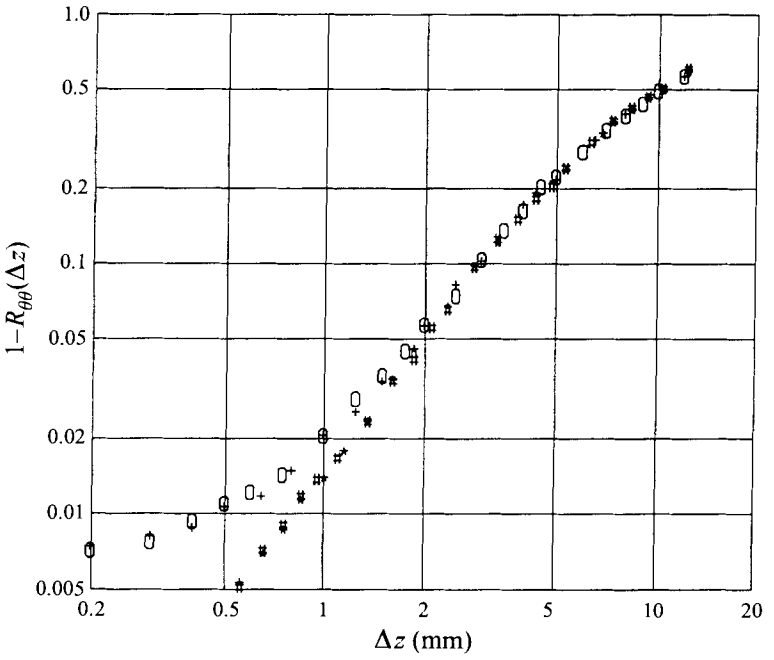

FIGURE 5. The effect of wire length, i.e. spatial resolution, on the cross-correlations for small separation distances of the two cold wires: 0, +, L_w of 1.25 mm and #, ⋆, L_w of 0.7 mm. The wire diameters were 1 μm and 0.65 μm respectively.

separation of the two wires. The length of the cold wires relative to the smallest wire separations influences the shape of the correlation curves, owing to the spatial resolution of each wire. We have briefly studied the effect of this resolution on the shape of the correlation curve for small separations. Figure 5 compares the correlation coefficients for two different wire lengths, 1.25 mm and 0.7 mm, with wire diameters of 1 μm and 0.65 μm, respectively, giving in both cases about the same length-to-diameter ratio. These measurements were taken simultaneously at the same down-stream location in the wind tunnel. The Batchelor scale at that location was about 0.5 mm. The longer-wire data clearly do not follow the above-mentioned power-law owing to the insufficient spatial resolution. The shorter wire, on the other hand, has evidently sufficient resolution.

3. Statistical relations for isotropic scalar fluctuations

3.1. *The growth of scalar fluctuations*

The scalar fluctuations in this experiment are produced by the turbulence-generating grid as the turbulent motions move fluid elements against the background mean vertical temperature profile. This generation mechanism is significantly different from the procedure used in generating the turbulent scalar fields in many previous studies, where the fluctuations are produced by passing the flow through a heated grid, as reviewed by Warhaft & Lumley (1978).

For heated grid experiments the fluctuations are generated at the grid and then decay monotonically downstream due to molecular mixing and associated dissipation of scalar fluctuations. Here, on the other hand, the initial scalar fluctuations are generated by the grid but continue to be generated farther downstream by the largest

eddies, as they pull in less-mixed fluid elements from farther away in the density gradient until an equilibrium is established between this density flux (stirring) and the molecular mixing. Corrsin (1952) has shown that in the passively stratified case without molecular mixing the scalar fluctuations would continue growing indefinitely. In the stably stratified case this continuing generation of scalar fluctuations is arrested by the buoyancy forces, which inhibit the vertical movement of the fluid elements. The dynamical equations for stratified flows thus contain an additional buoyancy flux term and the effect of the stratification on this heat flux is of major importance for the stirring and persistence of the scalar fluctuations.

3.2. *The balance of scalar variance*

For our experimental setup the dynamical evolution of the variance of the temperature fluctuations at each location downstream from the grid is determined by the competing elements of convection of these fluctuations by the mean flow, the generation of temperature fluctuations by the buoyancy flux working against (or with) the mean gradient and the molecular dissipation of scalar variance, as described by the following equation (see e.g. Van Atta 1985) which was derived assuming homogeneity in the vertical direction:

$$U\frac{\partial}{\partial x}\overline{\theta^2} = -2\overline{w\theta}\frac{\mathrm{d}T}{\mathrm{d}z} - \chi. \tag{3.1}$$

The scalar dissipation has the form

$$\chi = 2\alpha\left[\overline{\left(\frac{\partial\theta}{\partial x}\right)^2} + \overline{\left(\frac{\partial\theta}{\partial y}\right)^2} + \overline{\left(\frac{\partial\theta}{\partial z}\right)^2}\right] \tag{3.2}$$

where α is the thermal diffusivity. The mean temperature at each measurement location and daily atmospheric pressure were used to empirically calculate α. Isotropic turbulent scalar fields have direction-independent mean-square scalar gradients due to the rotational symmetry. It is therefore sufficient for isotropic fields to measure only one of the three gradients (usually the streamwise gradient using Taylor's hypothesis), from which the scalar dissipation is then given by the isotropic relation

$$\chi = 6\alpha\overline{\left(\frac{\partial\theta}{\partial x}\right)^2}. \tag{3.3}$$

Since we have measured all three terms in the balance equation (3.1), its closure can be assessed directly as will be done in §4.4.

3.3. *Temperature-gradient correlations and spectral relations*

The spatial correlation of the fluctuating temperature θ is direction independent for isotropic scalar fields, thus $R_{\theta\theta}(\Delta z) = R_{\theta\theta}(\Delta x)$. The same is not true for the spatial correlation of the gradients of temperature, since the gradient of a scalar field is a vector with components both along and perpendicular to the separation vector. Figure 6 shows the general correlation setup for the temperature-gradient correlations with a spatial separation in x or z. For isotropy, the two cases shown in figure 6 have identical statistics if one specifies whether the temperature derivative is in the direction of the separation vector, $\boldsymbol{B}_{\ell\ell}(\Delta x)$, or perpendicular to it, $\boldsymbol{B}_{nn}(\Delta x)$. Therefore

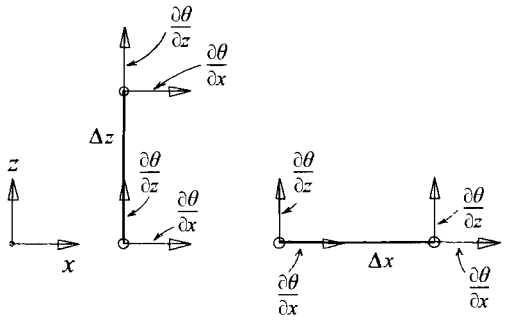

FIGURE 6. The relative orientation of the measured temperature gradients and the separation vector.

for separation in the x-direction the longitudinal correlation is defined as

$$B_{\ell\ell}(\Delta x) = \frac{\overline{\frac{\partial\theta}{\partial x}(x)\frac{\partial\theta}{\partial x}(x+\Delta x)}}{\overline{\left(\frac{\partial\theta}{\partial x}\right)^2}} \tag{3.4}$$

whereas the transverse (normal) correlation is

$$B_{nn}(\Delta x) = \frac{\overline{\frac{\partial\theta}{\partial z}(x)\frac{\partial\theta}{\partial z}(x+\Delta x)}}{\overline{\left(\frac{\partial\theta}{\partial z}\right)^2}}. \tag{3.5}$$

These two correlations are related by an isotropic relation derived by Obukhov (1954). We follow here the notation of Panchev (1971), for an arbitrary separation vector $\boldsymbol{r}$:

$$B_{\ell\ell}(\boldsymbol{r}) = B_{nn}(\boldsymbol{r}) + r\frac{\mathrm{d}}{\mathrm{d}r}B_{nn}(\boldsymbol{r}). \tag{3.6}$$

Note that this relation is fundamentally different from the one applying to the velocity correlations, as given by Taylor (1935):

$$g(r) = f(r) + \frac{r}{2}\frac{\mathrm{d}}{\mathrm{d}r}f(r). \tag{3.7}$$

where the conventional notation is used to identify $g(r)$ as the transverse and $f(r)$ as the longitudinal velocity correlations. The normal and longitudinal correlations are interchanged in (3.6) and (3.7) and the second term differs by a factor of $\frac{1}{2}$. The switching of the components arises because the velocity field is a divergence-free field ($\nabla\cdot\boldsymbol{u} = 0$), but the temperature-gradient field is curl-free, since $\nabla\times\nabla\theta(x,y,z)$ vanishes identically.

From the correlation tensor in equation (3.6) one can derive the corresponding spectral form relating the different gradient spectra to each other. These spectral relations between streamwise and vertical gradient spectra with respect to the streamwise wavenumber have been derived for the isotropic case by Panchev (1971) and independently by Van Atta (1977). The isotropic relation between the two gradient spectra

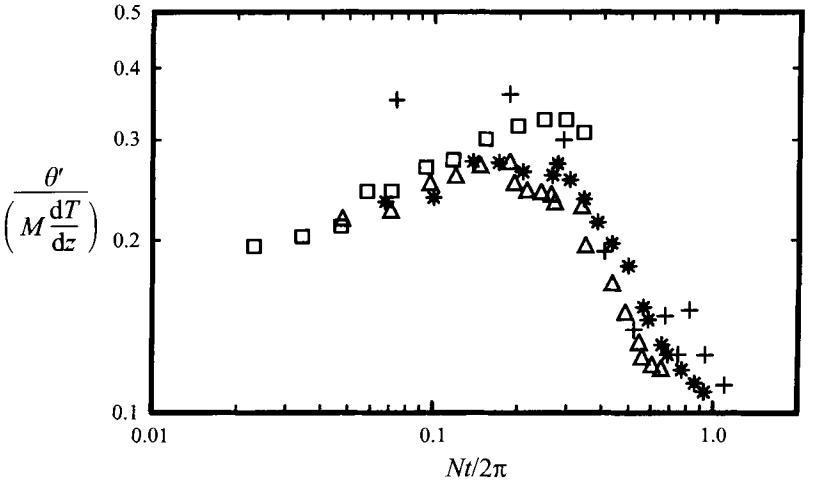

FIGURE 7. Temperature fluctuation levels for all four stratification strengths (rad s^{-1}). □, $N = 1.25$; △, $N = 2.53$; *, $N = 3.06$; +, $N = 4.03$.

is

$$E_{(\partial\theta/\partial z)(\partial\theta/\partial z)}(k_1) = \int_{k_1}^{\infty} \frac{1}{k} E_{(\partial\theta/\partial x)(\partial\theta/\partial x)}(k)\mathrm{d}k \tag{3.8}$$

where the wavenumbers are all taken to be in the streamwise x-direction. This relation can be integrated to predict the spectral shape of $E^P_{(\partial\theta/\partial z)(\partial\theta/\partial z)}(k_1)$ from the measured $E_{(\partial\theta/\partial x)(\partial\theta/\partial x)}(k_1)$ and to compare with the gradient spectrum $E_{(\partial\theta/\partial z)(\partial\theta/\partial z)}(k_1)$ measured by two coldwires, separated in z, as will be done in §4.5.

Relation (3.8) dictates that $E_{(\partial\theta/\partial z)(\partial\theta/\partial z)}(k_1)$ will reach a constant level† for small wavenumbers k_1 and then decrease monotonically with larger wavenumbers since the integrand in (3.8) is always positive. This is in sharp contrast to the shape of $E_{(\partial\theta/\partial x)(\partial\theta/\partial x)}(k_1)$, which is equal to $k_1^2\, E_{\theta\theta}(k_1)$, thus showing a local maximum at a large wavenumber and decreasing to zero for both the smallest and largest wavenumbers.

4. Results

4.1. *Temperature fluctuations and spectra*

Figure 7 shows the development of the temperature fluctuations for all four stratifications. For the weakest stratification the fluctuations grow strongly away from the grid and have just barely reached maximum by the end of the test section. The data for intermediate N values reach their maxima sooner, but display the same qualitative trends. However, for the strongest stratification ($N = 4$ rad s^{-1}) the fluctuations decay quickly and then rebound slightly before continuing to decay.

The downstream evolution of the temperature spectra is shown in figure 8. It shows that the small-scale, high-wavenumber energy is continuously eaten away by diffusion and the Batchelor scale grows continuously. Notice, however, that for the larger values of N the growth of scalar variance at the large scales is prohibited, whereas for the weakest one, $N = 1.25$ rad s^{-1}, the large-scale scalar variance continuously grows

† This requires that $E_{(\partial\theta/\partial x)(\partial\theta/\partial x)}(k_1)$ decrease faster than k for small k, which is indeed observed as $E_{\theta\theta}(k_1)$ is observed to be nearly constant as k approaches zero and the temperature-gradient spectrum in question is described by $k_1^2 E_{\theta\theta}(k_1)$.

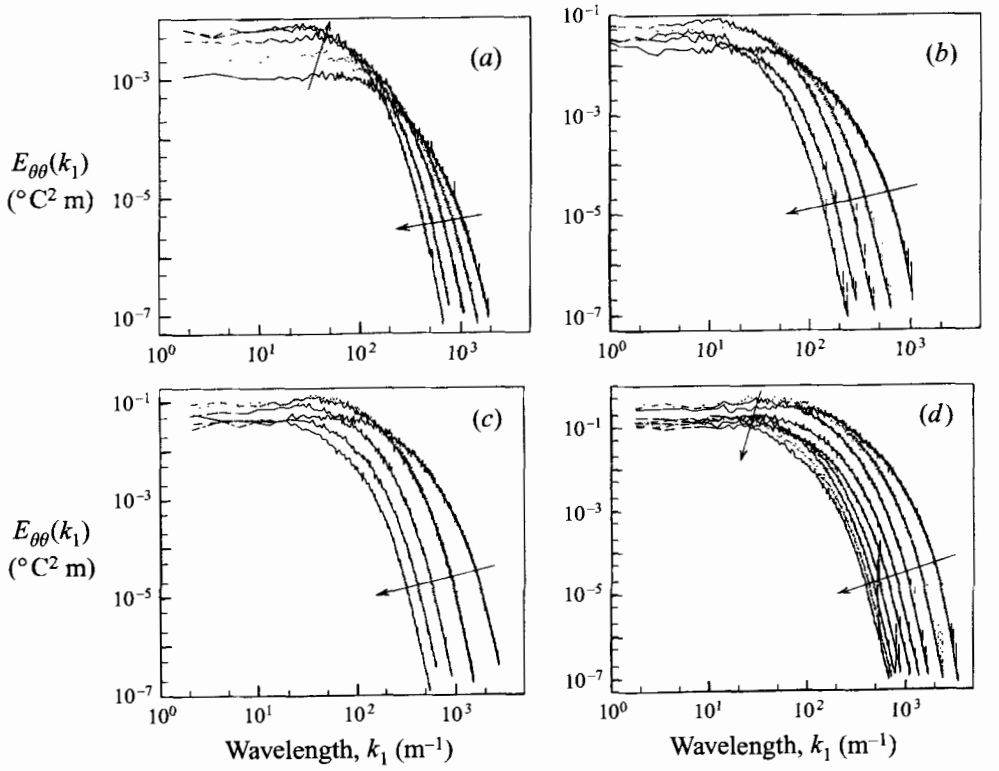

FIGURE 8. Temperature spectra for all four stratification strengths (rad s^{-1}) and many downstream locations. The arrows indicate the evolution of the spectra in the downstream direction. (*a*) N = 1.25 (x/M= 15, 30, 60, 100, 145); (*b*) N = 2.53 (x/M= 10, 30, 60, 100, 145); (*c*) N = 3.06 (x/M= 10, 30, 60, 100, 145); (*d*) N = 4.03 (x/M= 10, 23, 39, 55, 71, 90, 110, 125, 147).

downstream. This difference demonstrates clearly the presence of buoyancy effects, strong enough to limit vertical overturns. Spectra at all intermediate x/M follow the same trends.

The rebounding in the r.m.s. temperature levels, mentioned above, for N= 4 rad s^{-1}, could be caused by sufficiently strong restratification, or due to the generation of internal wave motions. The distinction between waves and turbulence is often based on the phase between w and θ, but since we did not measure w for the largest N this approach is not available. Some insight can however be obtained from the spectra of the θ fluctuations. These are shown in figure 8(*d*) for many downstream locations for the largest value of N. These spectra show slightly increased energy at frequencies larger than N. This energy may be due to production of 'evanescent' internal waves, which have frequencies greater than N, decay with distance from their source and do not obey the usual dispersion relation, as discussed, e.g., by Leblond & Mysak (1978, p. 72).

This increase is clearly different from the large-scale spectral signature of saturated internal waves discussed by Stillinger, Helland & Van Atta (1983) or Gibson (1980).

4.2. *Buoyancy flux*

The buoyancy-flux correlation coefficient is a sensitive gauge of the dynamical significance of the buoyancy forces. For passively stratified turbulence, e.g. Sirivat &

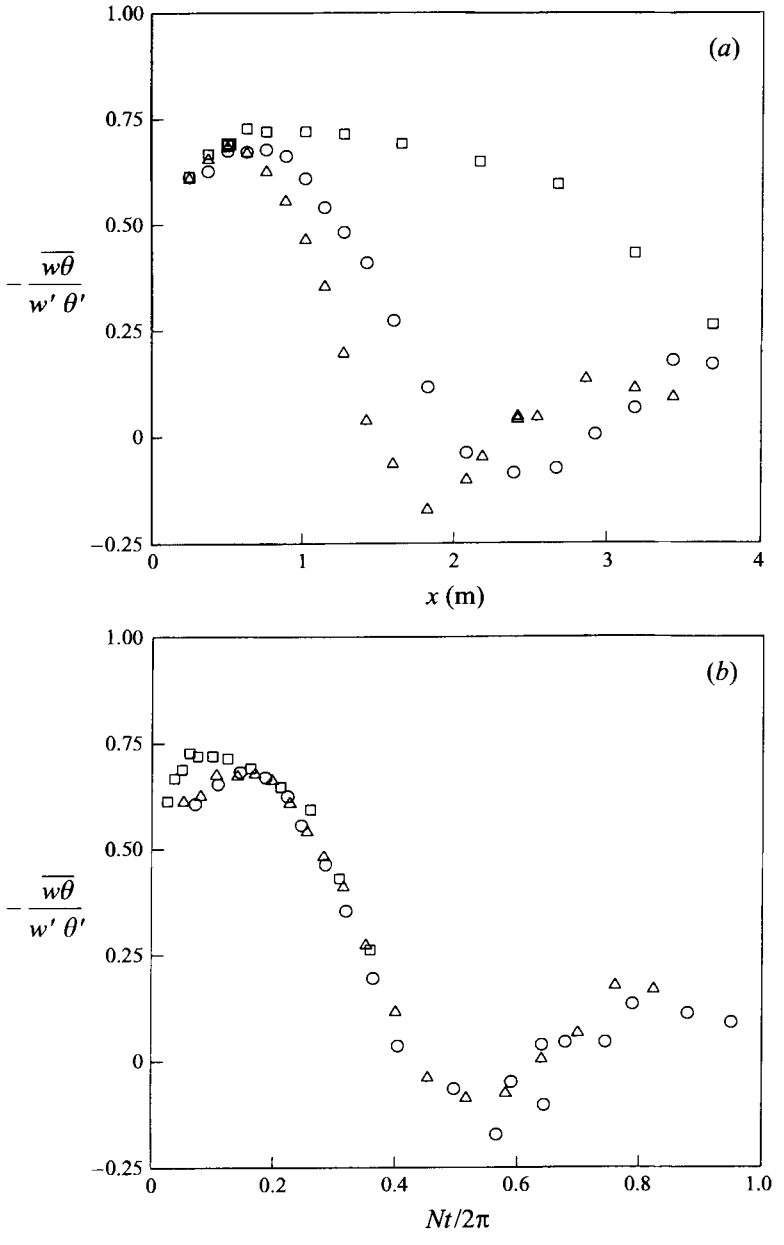

FIGURE 9. Buoyancy flux for N = 1.25 (□), 2.53 (○), 3.06 (rad s^{-1}) (△): (*a*) *vs.* x and (*b*) *vs.* Nt.

Warhaft (1983), the normalized buoyancy flux reaches a constant level of about 0.70 for the Prandtl number of our experiment. For the much larger Schmidt numbers in experiments using salt-stratified water this constant level for the buoyancy flux is cut by almost half, e.g. Stillinger *et al.* (1983) and Itsweire, Helland & Van Atta (1986). The buoyancy fluxes in figure 9 show that all our runs were actively stratified, i.e. the temperature cannot be considered a passive scalar, not even for the weakest stratification, since the buoyancy forces have started to inhibit the stirring, for the largest x/M, diminishing the buoyancy-flux correlation.

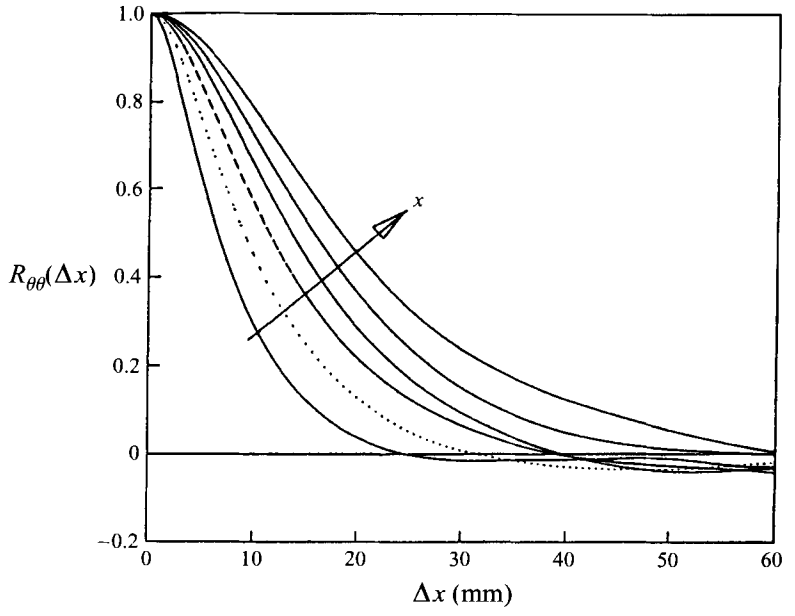

FIGURE 10. Typical downstream evolution of the streamwise auto-correlations of temperature for $N = 1.25$ (rad s^{-1}).

The buoyancy flux has been shown, by Lienhard & Van Atta (1990), to scale well with the buoyancy time Nt for similar initial turbulent Froude numbers. This is confirmed by our data in figure 9(*b*). The passive behaviour of the turbulence extends only up to $Nt/2\pi \simeq 0.15$. For the stronger stratifications the experiments also encompass the restratification regime, as demonstrated by a small countergradient flux, where $-\overline{w\theta} < 0$.

Since the turbulent velocities were not measured for the strongest stratification ($N = 4$ rad s^{-1}) owing to the experimental difficulties associated with the very large temperature fluctuations, the flux could not be estimated for that case.

4.3. *Mean-square temperature gradients*

4.3.1. *Auto- and cross-correlations*

The r.m.s. levels of $\partial\theta/\partial x$ and $\partial\theta/\partial z$ were estimated using the correlation method explained in §2.3. Figure 10 shows the development of the temperature auto-correlation curves, for the weakest stratification strength, obtained by the use of Taylor's hypothesis. Using numerous separations of the two wires, arranged according to the setup in figure 3(*b*), we calculated the temperature cross-correlations and plotted them on a log-log graph as explained in §2.3. Figure 11 shows the correlations for the strongest stratifications. The correlations follow the predicted functional form quite well over a range of separations, i.e. they follow a slope of 2 on the log-log graph. The adherence to this law is in quantitatively good agreement with the previous results of Browne *et al.* (1987). Since we took measurements for numerous Δz we had many different time-series to choose from for the linear fit for the Δx separations. In figure 4 all of the Δx-correlations were included, giving an indication of their spread. To include some indication of the effects of this variability of the auto-correlations on the estimate of the strain-rate ratios, we integrated all of these auto-correlation curves

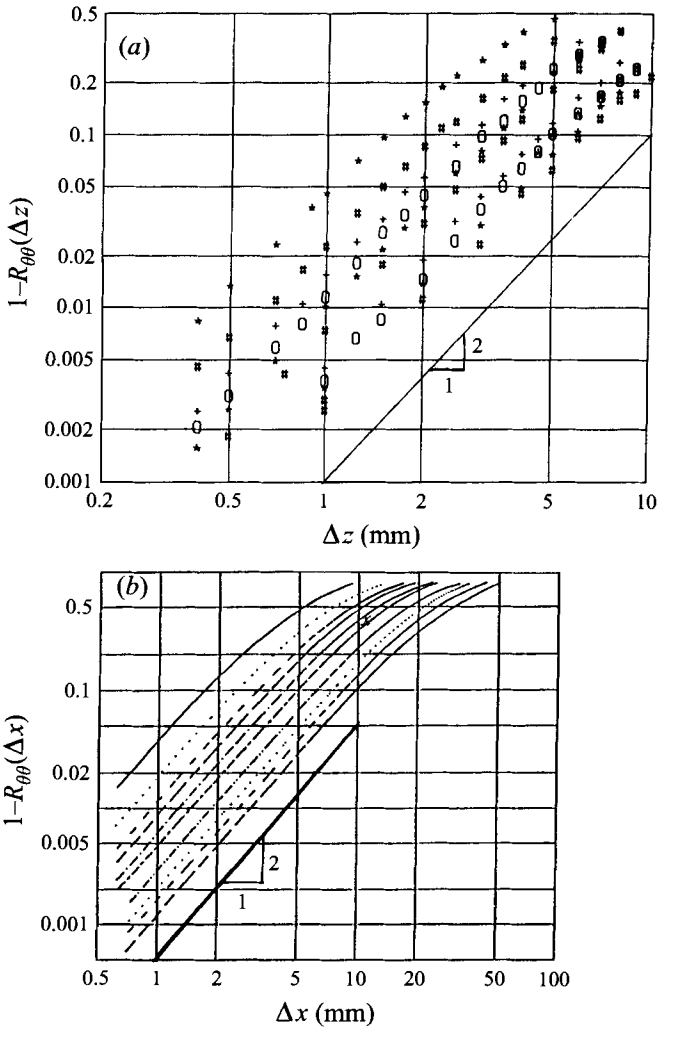

FIGURE 11. Auto- and cross-correlations of temperature plotted in a log-log format for evaluation of mean-square strain rates using the correlation method, $N = 4.03$ rad s^{-1} for $x/M =$ 10, 20, 30, 40, 55, 70, 90, 110, 125, 147. (*a*) Cross-correlations, for many separations Δz. Each symbol shows results for a different downstream location x. The top curve shows results for the x-location closest to the grid. (*b*) Auto-correlations using Taylor's hypothesis to change Δx.

to obtain integral length scales and used the curve which had the median integral length scale to estimate the gradients. The curves giving the maximum and minimum integral scales were also used as an upper limit for the error due to inaccuracies in the auto-correlation estimates. This estimate has been included in figure 12. This variability is primarily caused by the limited time-series length collected for each separation Δz, which was kept as short as possible because we wanted to limit any effects of long-term drift in the facility. The sample length had, on the other hand, to be long enough to get acceptable convergence of the correlation statistics. The resulting compromise of 27 seconds showed sufficient convergence in the $R_{\theta\theta}(\Delta z)$, as is demonstrated in the Appendix.

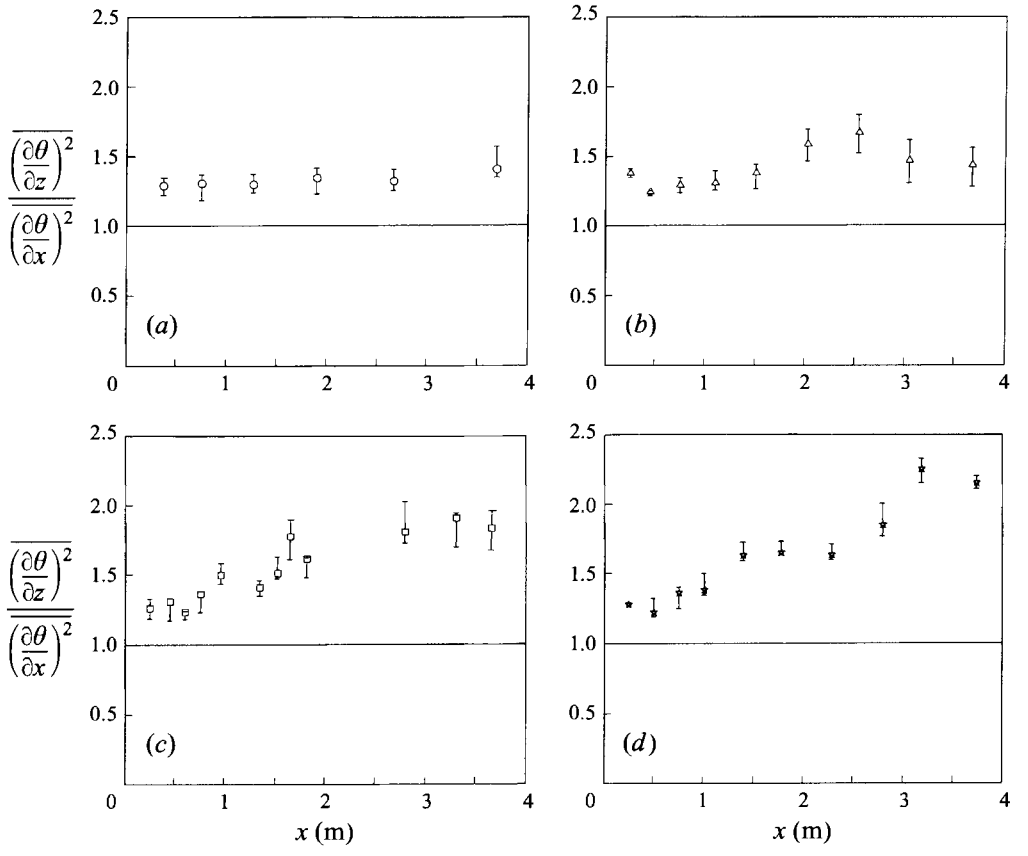

FIGURE 12. The mean-square temperature gradient vertical anisotropy ratios for all stratifications (rad s^{-1}): (*a*) $N = 1.25$; (*b*) $N = 2.53$; (*c*) $N = 3.06$; (*d*) $N = 4.03$.

4.3.2. *Temperature-gradient anisotropies*

The gradient anisotropy was evaluated by comparing the mean-square values of $\partial\theta/\partial x$, $\partial\theta/\partial y$ and $\partial\theta/\partial z$. Figure 12 shows the evolution of the ratio of the mean-square temperature gradients in the vertical and streamwise directions for all four N. The ratio is initially about 15% larger than the isotropic value of 1.0 and anisotropy grows downstream of the grid. This continually growing scalar gradient anisotropy contrasts with the arrested anisotropic behaviour we observed earlier for velocity gradients (Thoroddsen & Van Atta 1989, 1992*a*), in which the ratios of r.m.s. velocity gradients reached maximum values or even returned toward isotropic values far downstream. As for the earlier case of the velocity gradients, the stronger the stratification, the stronger the temperature-gradient anisotropy. Figure 13 shows the ratio of the previous figure, now scaled with the buoyancy time. The initial anisotropy collapses around one curve showing that it initially develops approximately linearly with buoyancy time. The trends are consistent for the different stratification strengths and the brief apparent reversal in the trend starting at $Nt/2\pi \approx 0.5$ is directly associated with the restratification region as shown in figure 9(*b*). The most anisotropic behaviour of this ratio shows a value of about 2.2 for the largest Nt.

Figure 13 includes DNS results from Gerz & Schumann (1991). These results are qualitatively similar, but anisotropies develop much more quickly than in the

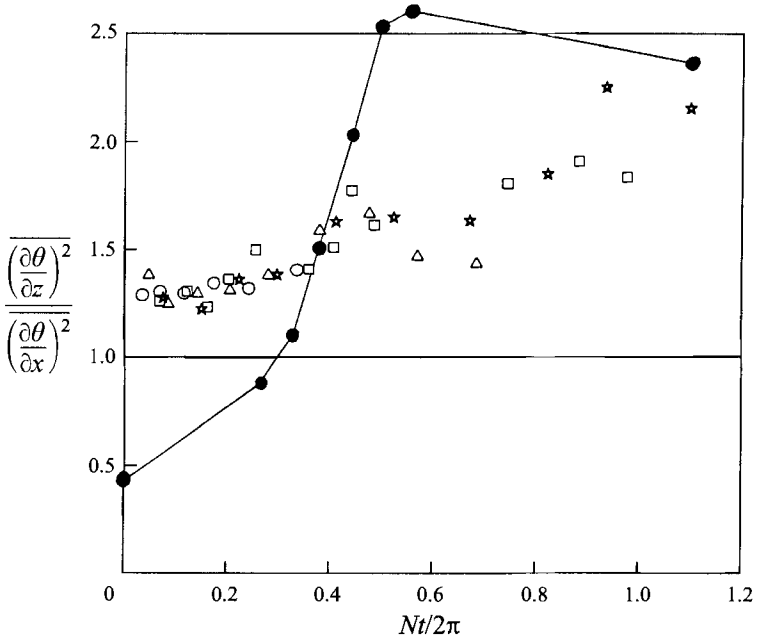

FIGURE 13. The vertical gradient anisotropy ratios of figure 12 now scaled *vs.* buoyancy time Nt. The solid line connecting filled circles shows results from the numerical simulations of Gerz & Schumann (1991).

experiments. This may be due to the different initial conditions evident in the figure, which show that the numerical simulations have been started from a highly anisotropic state.

Closest to the grid the vertical gradients are somewhat larger than the streamwise ones. This is probably due to the anisotropy in the grid-generation mechanism, evident so close to the grid. This is supported by the slight dip in the curves at $Nt \approx 0.1$, which indicates isotropization immediately after the flow leaves the grid and before buoyancy effects become significant.

The cross-stream horizontal gradients were also measured for one of the stratifications, $N = 2.53$ rad s^{-1} and the corresponding ratio is shown in figure 14. The horizontal cross-stream gradient shows much smaller anisotropies than the vertical one, especially far downstream. This is consistent with buoyancy forces being the cause of the vertical anisotropy.

It should be mentioned here that Thoroddsen & Van Atta (1992*b*) found that the probability density function of $\partial\theta/\partial z$ is skewed in the direction of the mean vertical heat flux and they constructed a simple model, based on the mean flux, to explain this skewness. This skewness, which was shown not to be caused by buoyancy forces, does not directly affect the current discussion of anisotropy caused by buoyancy, since we are here studying an even moment of the density gradient field.

Tong & Warhaft (1994) have recently verified and studied this temperature-gradient skewness.

4.3.3. *The anisotropy of dissipation estimates*

Using the measured temperature-gradient values presented above, we can estimate the accuracy of the dissipation value deduced from only one of those gradients

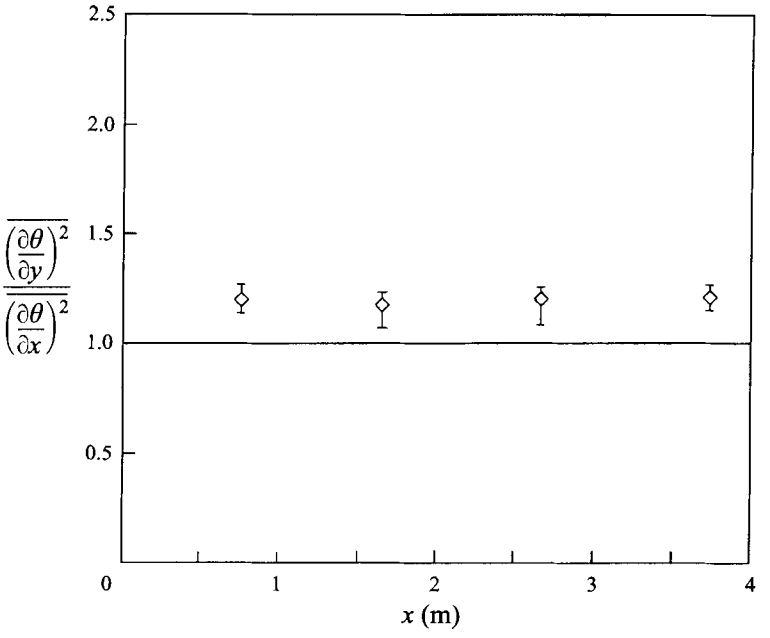

FIGURE 14. The transverse horizontal temperature-gradient anisotropy, for $N = 2.53$ rad s^{-1}.

assuming isotropy. To this end, the streamwise temperature-gradient spectra were integrated to obtain an estimate of the scalar dissipation rate χ based on $\partial\theta/\partial x$ through the assumption of isotropy (equation (3.3)). The integration was interactively performed on a graphics computer terminal allowing for the inclusion of all significant energy above the noise level and the removal of any 60 Hz spikes and their higher harmonics from the spectra. The spectra were in general very clean and free of noise spikes, as is shown in figure 8. Figure 15 shows this χ for all of the stratifications, and includes both an estimate based on $(\partial\theta/\partial x)^2$ along with isotropy, as well as an estimate combining all three temperature gradients based on figure 12. The r.m.s. lateral temperature gradients $(\partial\theta/\partial y)$ were only measured for one of the stratification strengths, i.e. $N = 2.53$ rad s^{-1}. However, figure 14 showed that the lateral gradient was only slightly affected by the buoyancy. It can therefore be reliably estimated as a fixed proportion of the $\partial\theta/\partial x$ gradient. This factor is estimated as 1.17 from figure 14.

It can be deduced from the anisotropy results presented in the previous subsection that if one were to base the dissipation estimate on the streamwise gradient $\partial\theta/\partial x$ one would underestimate χ by up to 40%, but basing it on $\partial\theta/\partial z$ would on the other hand overestimate χ by up to 40%, for the largest Nt in our experiments.

4.4. *Closure of the scalar variance budget*

Having measured all the terms in equation (3.1) we can now attempt to verify its closure. We define D as

$$D = U\frac{\partial}{\partial x}\overline{\theta^2} + 2\overline{w\theta}\frac{\mathrm{d}T}{\mathrm{d}z} + \chi. \tag{4.1}$$

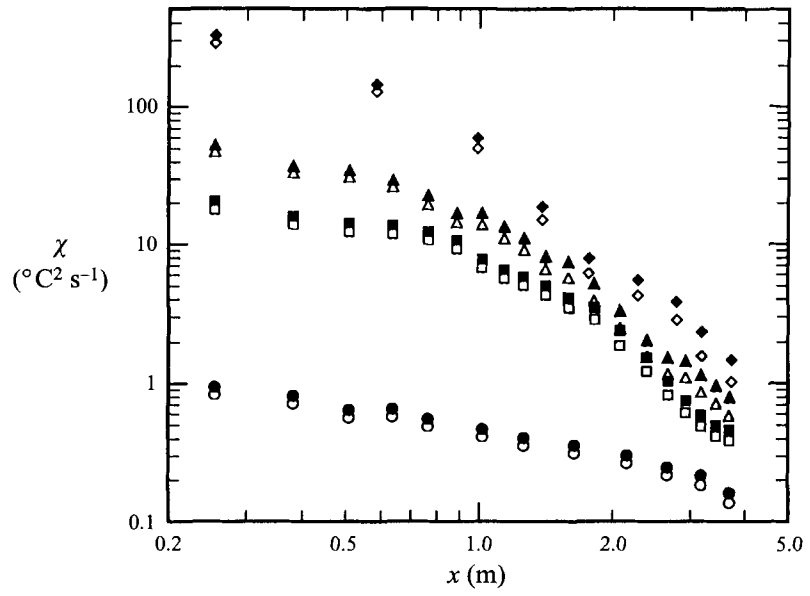

FIGURE 15. Temperature dissipation rates for all four stratification strengths (rad s^{-1}); N = 1.25 (○), 2.53 (□), 3.06 (△) and 4.03 (◇). The open symbols show results based on $\partial\theta/\partial x$ using isotropy, whereas the solid symbols are based on the current estimates of the values of all three temperature gradients.

We have plotted the individual terms in the above relation in figure 16. Looking at previous experimental results one notices that, close to the grid, neither Lienhard & Van Atta (1990) nor Yoon & Warhaft (1990) have achieved closure of the temperature variance balance, as shown in figure 16, but rather show discrepancies as large as 115% and 90%, respectively, based on the scalar dissipation rates closest to the grids, i.e. D/χ_o.

Our results for the individual temperature gradients show that, close to the grids, the isotropic dissipation relation is most applicable, the dissipation based on the isotropic relation being only about 15% from the actual measured value based on all three of the gradients. This suggests that the lack of closure of the scalar variance balance observed in the two above-mentioned studies is not due to the inaccuracies incurred by estimating the scalar dissipation rate based on isotropy. A probable explanation is rather the attenuation of the temperature fluctuations due to prong effects. This attenuation is due to the small length-to-diameter ratios ($L_w/D_w \simeq 400$) of the cold-wires used in those studies. This dynamic attenuation of the fluctuating temperature is not simply a scale factor altering the entire balance in (3.1), since there is a static term involved, i.e. the term including the factor dT/dz. Figure 16(c) shows the closure achieved here for N = 2.5 rad s^{-1}. The closure for the other N values was similar. The much better closure achieved here by using $L_w/D_w \simeq 1100$ certainly indicates that the above deviations are due to prong effects. These conjectures are in accordance with careful studies by Browne & Antonia (1987) designed to quantify the prong effects. The streamwise gradient in equation (3.1) was estimated from a fifth-order polynomial fit to the $\overline{\theta^2}$ *vs.* x curves and χ was estimated from the isotropic relation for consistency in the comparison with the other researchers. These results

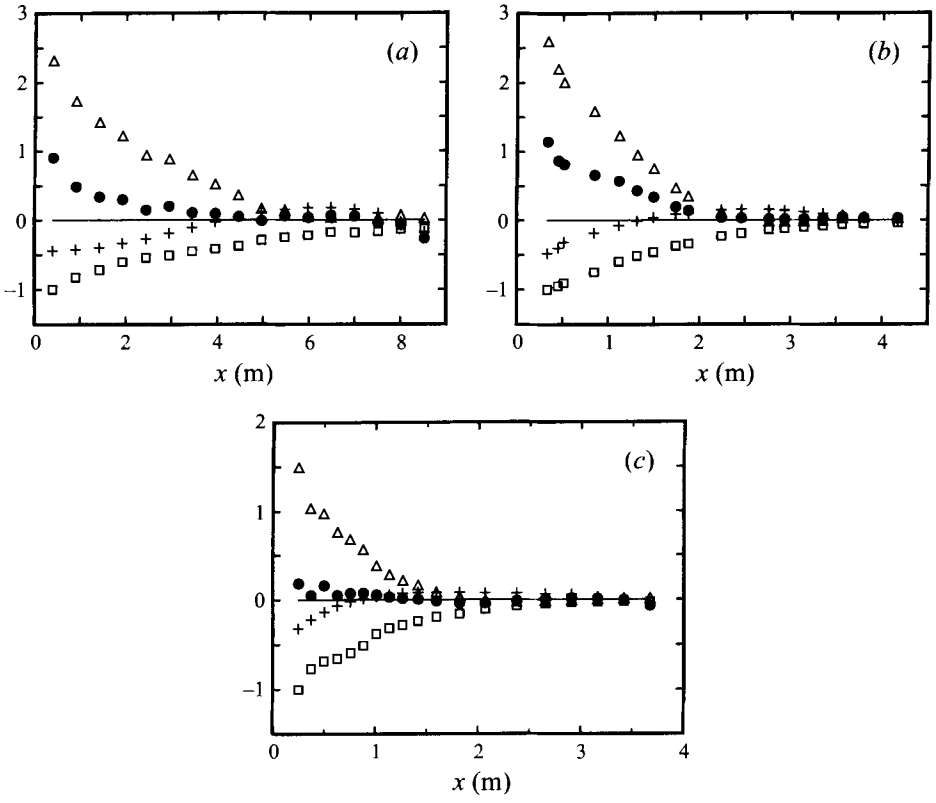

FIGURE 16. Closure of the scalar variance balance: the various terms in equation (4.1), normalized by the dissipation close to the gid χ_o. •, balance D/χ_o; □, scalar dissipation; +, advection; △, buoyancy flux. (*a*) Yoon & Warhaft (1990), (*b*) Lienhard & Van Atta (1990), (*c*) current balance.

give us added confidence that we have, in the current experiments, accurately resolved all of the scalar gradient fluctuations.

4.5. *Temperature-gradient spectra*

Following the discussion in §3.3 the spectral relations between the different temperature-gradient spectra were also studied. We first estimated the sensitivity of the gradient spectrum $E_{(\partial\theta/\partial z)(\partial\theta/\partial z)}(k_1)$ to the separation distance of the two wires used in its estimate. Figure 17 shows the vertical gradient spectra calculated for four different separations of the cold wires, at $x/M = 80$ where $\eta_\theta = 1.5$ mm. The data shown in this figure have not been filtered, to show the background noise level of the instrumentation. The only differences observed between the respective spectra are at the highest frequencies. For larger separations the energy at high frequencies is larger. This behaviour may be understood as follows. Making a Taylor series expansion of the temperature at the second cold wire in terms of the temperature and its spatial derivatives at the first cold wire, the measured temperature gradient is, up to second-order terms in Δz,

$$\left(\frac{\partial\theta}{\partial z}\right)_m = \frac{\partial\theta}{\partial z} + \frac{\partial^2\theta}{\partial z^2}\frac{\Delta z}{2} + \frac{(n_1 - n_2)}{\Delta z} \tag{4.2}$$

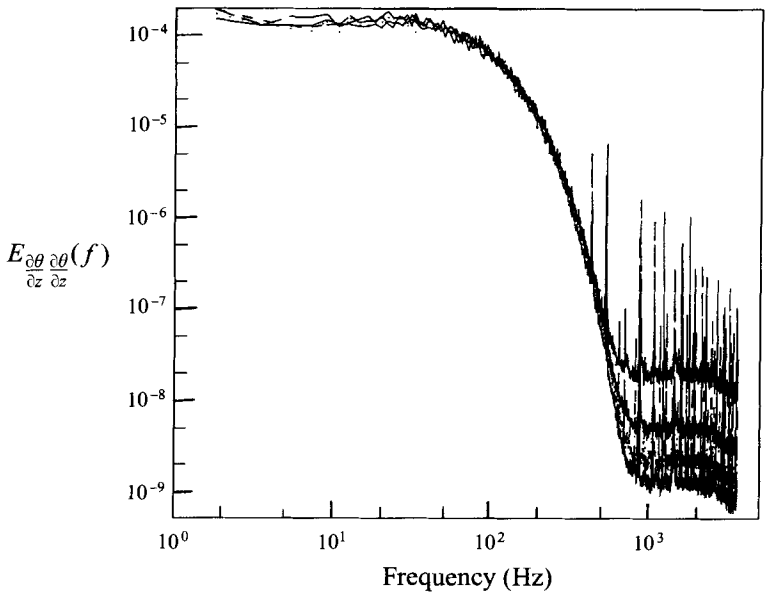

FIGURE 17. Spectra of the vertical temperature gradients *vs.* wavenumber obtained using different separations of the coldwires, $\Delta z = 2$, 4, 6 and 8 mm. The spectra have not been filtered to show the noise levels in the measurements. The spectrum showing the lowest 'noise'-level on the figure corresponds to the 2 mm separation. Larger Δz show progressively larger energy levels at high wavenumbers, as discussed in the text.

where $\partial\theta/\partial z$ and $\partial^2\theta/\partial z^2$ are the true temperature gradient and its spatial derivative in the direction of Δz, respectively, and n_1 and n_2 are the electronic noise signals for the two cold wires, respectively. Assuming that $\partial\theta/\partial z$ and $\partial^2\theta/\partial z^2$ are uncorrelated, and that the temperature field and the electronic noise contributions are uncorrelated, the measured mean-square temperature derivative is

$$\overline{\left(\frac{\partial\theta}{\partial z}\right)_m^2} = \overline{\left(\frac{\partial\theta}{\partial z}\right)^2} + \overline{\left(\frac{\partial^2\theta}{\partial z^2}\right)}\frac{(\Delta z)^2}{4} + \frac{\overline{(n_1 - n_2)^2}}{(\Delta z)^2}. \tag{4.3}$$

Note that the contribution from the mean-square second-derivative increases with increasing Δz, consistent with the trend of the data, while the noise contribution decreases with increasing Δz. In terms of spectra, and assuming that the noise contributions are negligible, we have

$$\left[E_{(\partial\theta/\partial z)(\partial\theta/\partial z)}(k_1)\right]_m = E_{(\partial\theta/\partial z)(\partial\theta/\partial z)}(k_1) + E_{(\partial^2\theta/\partial z^2)(\partial^2\theta/\partial z^2)}(k_1)\frac{(\Delta z)^2}{4}. \tag{4.4}$$

Since the high-frequency spectral energy spectral levels are nearly independent of frequency, the argument can now be completed in terms of either mean-square values or spectra. At high frequencies the true spectrum gives a negligible contribution and the major contribution comes from the mean-square second-derivative term, which scales like the square of Δz.

Equation (4.4) thus predicts that the ratio of the spectral levels for $\Delta z = 4$, 6 and 8 mm to those for $\Delta z = 2$ mm should be 4, 9, and 16, respectively. The measured ratios from figure 17 are 2, 5 and 16, respectively, so the above analysis accounts fairly well for the observed behaviour. Cross-talk noise between the wires would reduce the increase predicted by the above analysis.

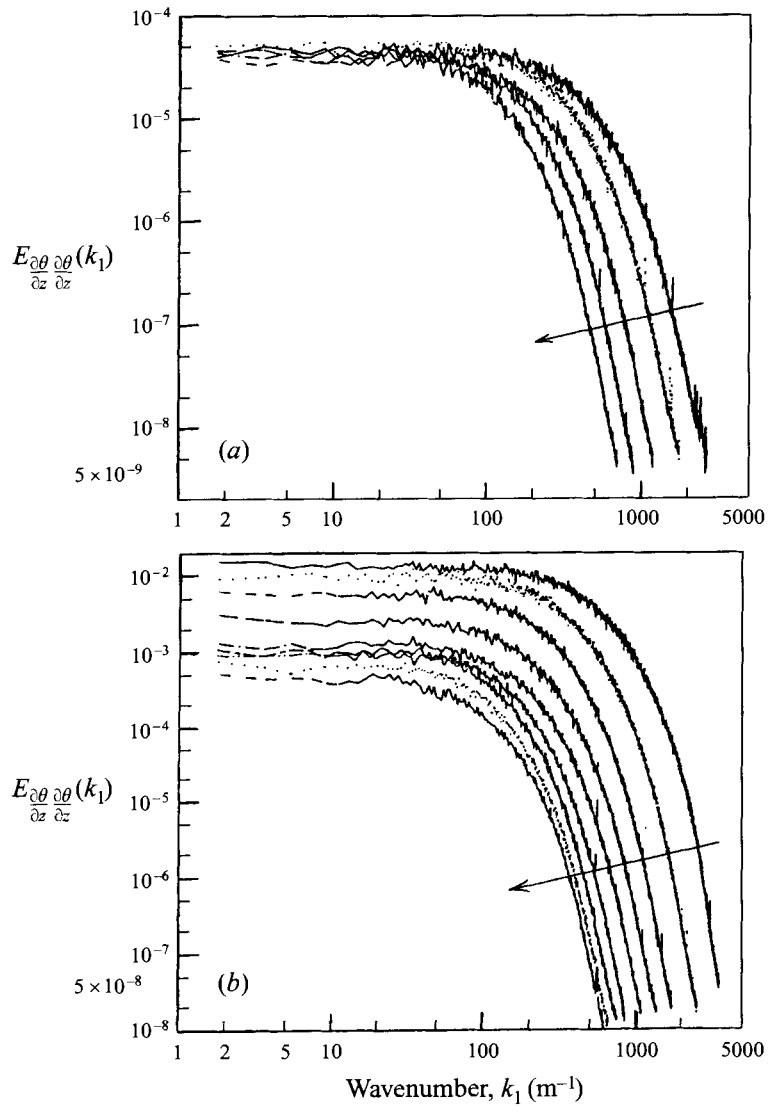

FIGURE 18. Spectra of $\partial\theta/\partial z$ *vs.* downstream location (ordinate in arbitrary units). (*a*) $N = 1.25$ (rad s^{-1}) (x/M= 15, 30, 60, 100, 145) and (*b*) $N = 4.03$ rad s^{-1} (x/M= 10, 23, 39, 55, 71, 90, 110, 125, 147).

Figure 18 shows the evolution of the vertical gradient spectrum *vs.* downstream location for the weakest and strongest stratifications studied. The large-wavenumber contributions to the gradient are most quickly destroyed by molecular diffusion for both of these stratification strengths, i.e. the scalar diffusion dissipates the energy of temperature fluctuations at the smallest scales and the Batchelor scale grows. For the strongest stratifications there is also a monotonic decline in energy at the large scales, whereas for the weakest stratification the large-scale gradients retain most of their energy.

The relations between the different gradient spectra discussed in §3.3 were next studied. Equation (3.8) was integrated to predict $E_{(\partial\theta/\partial z)(\partial\theta/\partial z)}(k_1)$ from the measured $E_{(\partial\theta/\partial x)(\partial\theta/\partial x)}(k_1)$. Figure 19(*a–d*) shows a set of measured and predicted $E_{(\partial\theta/\partial z)(\partial\theta/\partial z)}$ for

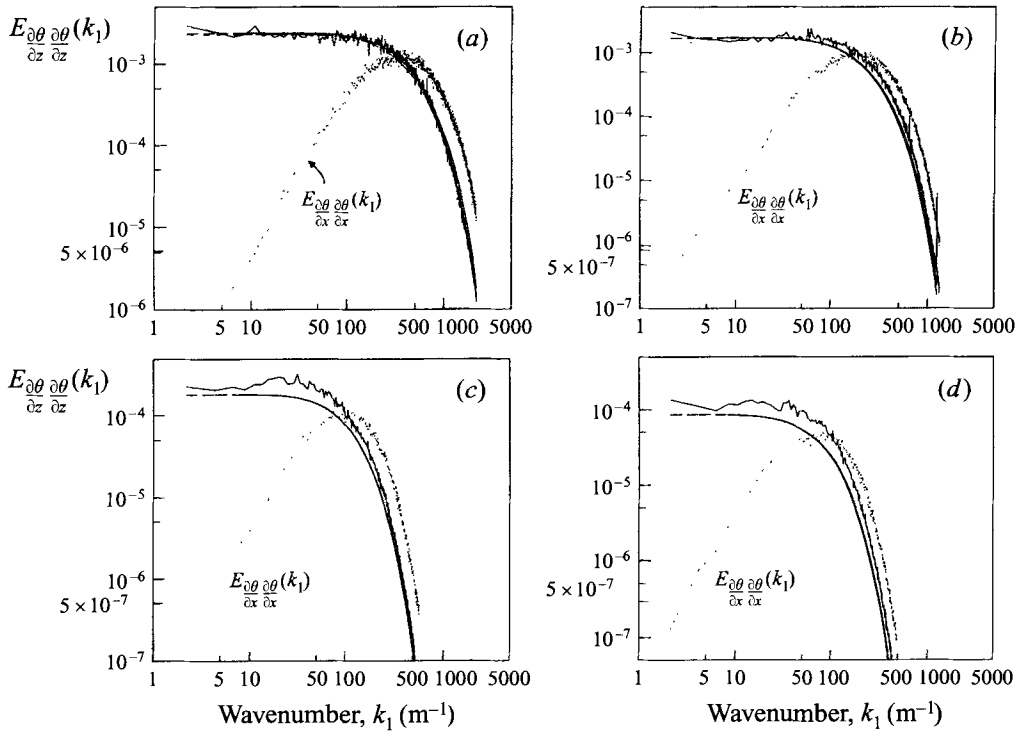

FIGURE 19. Measured and predicted vertical temperature gradient spectra (ordinate in arbitrary units), for N = 3.06 rad s^{-1}, x/M = (*a*) 15, (*b*) 40, (*c*) 100, (*d*) 150. The dotted line shows the measured spectrum of the streamwise temperature gradient. The two smooth solid lines show the predicted spectrum, using equation (3.8), of the vertical temperature gradient. The jagged solid line shows the corresponding measured spectrum of the vertical temperature gradient.

different downstream locations for N= 3.06 rad s^{-1}. The isotropic relations hold quite well near the grid, but farther downstream the spectrum becomes strongly anisotropic. Interestingly, anisotropy is observed at all scales. For very large Reynolds numbers the conventional expectation is that the large scales will first feel the stratification and develop anisotropies before the small scales, in accordance with the notion of a cascade. The data show that for the present Reynolds number all scales develop anisotropies at about the same rate. The relatively low Reynolds number of the present experiments and the uncertainties associated with the sensitivity of $\partial\theta/\partial z$ to the separation of the wires as shown in figure 17 preclude clear determination of which scales feel the stratification first. Measurements or DNS at larger Re_λ would be useful to resolve this dilemma.

It should be noted that the spectral composition of the gradient anisotropy has here been studied by looking at the $E_{(\partial\theta/\partial z)(\partial\theta/\partial z)}(k_1)$-spectra instead of the $E_{(\partial\theta/\partial z)(\partial\theta/\partial z)}(k_3)$-spectra. These two spectra will have different shapes (see §3.4), but their total variance is the same, as

$$\overline{\left(\frac{\partial\theta}{\partial z}\right)^2} = \int_0^\infty E_{(\partial\theta/\partial z)(\partial\theta/\partial z)}(k_3)\mathrm{d}k_3 = \int_0^\infty E_{(\partial\theta/\partial z)(\partial\theta/\partial z)}(k_1)\mathrm{d}k_1. \tag{4.5}$$

To highlight the spectral composition of the gradient anisotropy, we have formed the ratio of the measured $E_{(\partial\theta/\partial z)(\partial\theta/\partial z)}(k_1)$ and the predicted spectrum $E^P_{(\partial\theta/\partial z)(\partial\theta/\partial z)}(k_1)$

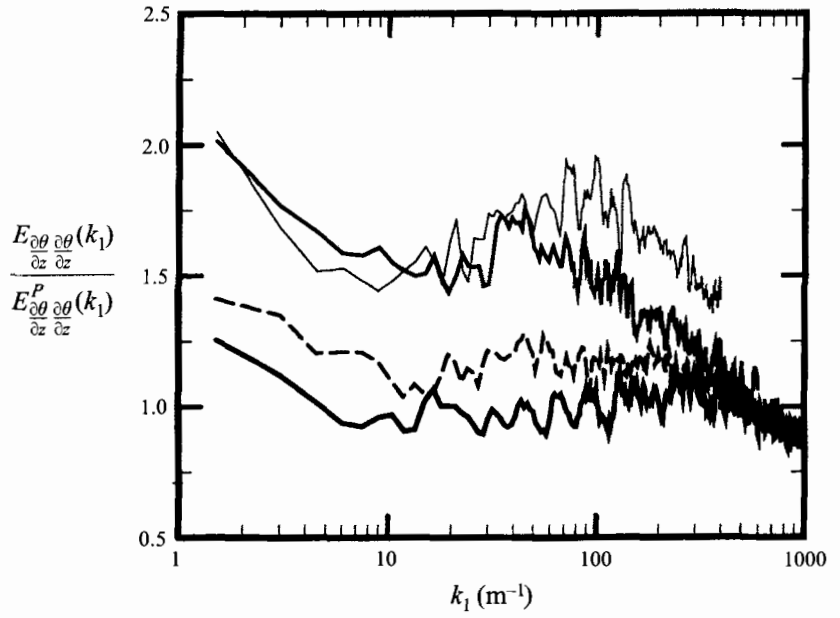

FIGURE 20. Ratios of the predicted and measured spectra of $\partial\theta/\partial z$, at different downstream loactions, corresponding to $Nt/2\pi = 0.15$ (thickest solid line); 0.30 (dashed line); 0.46 (medium thick line); 0.72 (thinnest line). $N = 2.53$ rad s^{-1}, $M = 2.54$ cm.

using the measured $E_{(\partial\theta/\partial x)(\partial\theta/\partial x)}(k_1)$. This ratio should therefore take the value of one for an isotropic temperature gradient field at every k. This ratio is shown in figure 20. Close to the grid the ratio is close to unity for all wavenumbers. For increasing Nt the anisotropy grows at all wavenumbers, but somewhat slower at the largest k.

5. Summary and conclusions

The 'correlation method' has been used to estimate the evolution of the mean-square values of the fluctuating temperature gradients, $\partial\theta/\partial x$, $\partial\theta/\partial z$ and $\partial\theta/\partial y$ for different stratification strengths and buoyancy times. Buoyancy forces were found to produce anisotropy in the fluctuation levels of $\partial\theta/\partial z$ relative to $\partial\theta/\partial x$ for large Nt, while the intensities of the two gradients in the horizontal plane remain nearly the same. The mean-square vertical gradient fluctuations observed here are as much as 2.2 times those for the streamwise gradient.

Using the measured values of the mean-square gradients we can estimate the accuracy of the isotropic dissipation estimates deduced from measurements of only one gradient. The results show that if one based the dissipation estimate on the isotropic formula using only $\partial\theta/\partial x$ or $\partial\theta/\partial z$ then χ would be respectively under- or overestimated by up to 40% for the largest Nt in our experiments. This discrepancy may continue to grow for even larger buoyancy times. This is consistent with recent LES by Chasnov (1996), at much larger Nt, which have shown a trend towards a fixed vertical integral length scale while the horizontal scale continues growing. The pancake-type structures observed in the late stages of decaying stably stratified turbulence also have this property. This is well illustrated in Turner's book (1973, figure 5.10) and by Koop & Browand (1979). Forced turbulence DNS by Herring & Métais (1989) have also revealed the formation of layered structure. Our

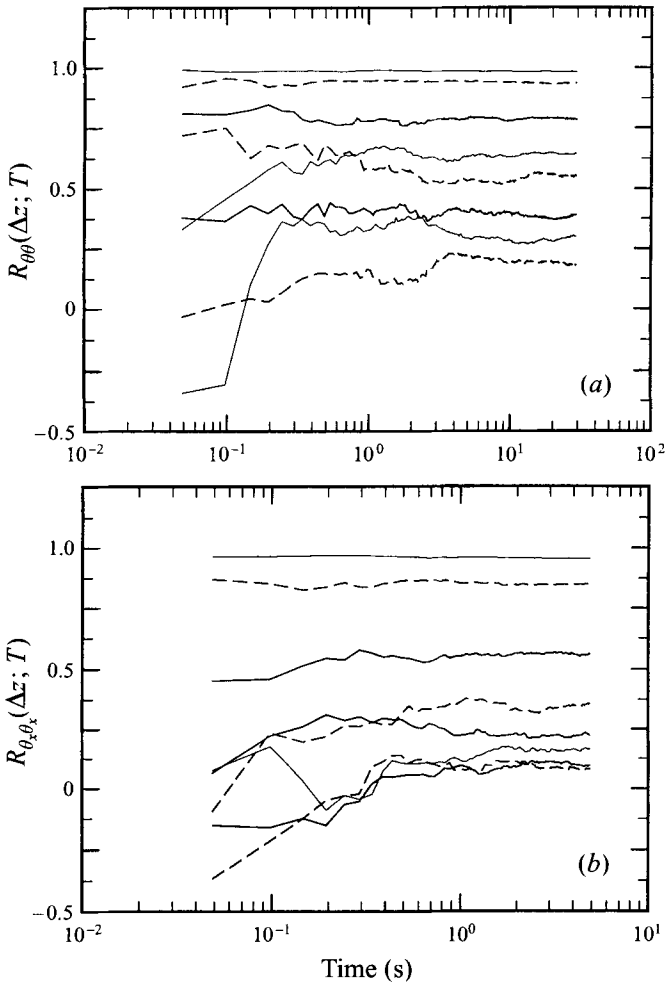

FIGURE 21. The convergence of cross-correlation values *vs.* length of averaging time. (*a*) The temperature correlation and (*b*) the correlation of temperature gradients. The convergence is portrayed for numerous separations of the two cold wires, showing the convergence for various correlation values. Note the different extent of the two time-axes.

measurements thus give valuable information regarding how quickly the buoyancy-affected turbulence develops into a highly anisotropic form after a violent turbulence-generating event, such as internal wave breaking.

The numerical simulations of Itsweire *et al.* (1993) have studied the vertical density-gradient anisotropy of stratified uniform-gradient shear flow. They find an average ratio of mean-square temperature gradients in the vertical and streamwise directions of 6.5, which is much larger than we see here. This much larger ratio may be caused both by the shear, which is zero in our experiments, and the initial large anisotropy of the small scales in their DNS as compared with the initial near isotropy of the present experiments.

The temperature gradient spectra are suppressed by buoyancy at all scales, not just at the large scales, as was demonstrated by comparing the measured spectra with the predicted vertical gradient spectra. This behaviour might be due to a Reynolds

number which may not be sufficiently large for dynamical separation of large and small scales ($Re_\lambda \simeq 20$), or it could be indicative of a more fundamental behaviour of strongly buoyancy-affected turbulence. It would therefore be of interest to measure this anisotropy for larger Reynolds numbers, where the separation of scales is more significant.

The authors thank Professors Zellman Warhaft and John H. Lienhard V for enlightening discussions. We thank Frank Petach for his help with constructing the cold wires. This work was supported by ONR Contract # N00014-94-1-0233 and NSF grant OCE92-17213. S.T.T. received financial support from the University of Illinois Research Board. Some of the present spectral results were previously reported by Van Atta (1991).

Appendix

In this Appendix we describe experimental results demonstrating the convergence of statistical quantities. The convergence rates were used to decide what averaging time to use in constructing correlation curves. Figure 21 shows measured values of the two-point correlations of temperature and temperature gradients versus the time-series length used in their evaluation. The figure shows the convergence rate for numerous correlation levels between the two temperature signals in figure 21(*a*) as well as between the temperature-gradient signals in figure 21(*b*). The least-correlated signals exhibit the slowest convergence and the gradient correlations converge faster than the temperature, owing to the higher frequency contents of the gradients. Note the different extent of the time axes for the two graphs in figure 21. Based on these results, the averaging time used in the actual correlation estimates was chosen as 27 seconds, corresponding to approximately 2500 integral time scales.

REFERENCES

BATCHELOR, G. K. 1959 Small-scale variation of convected quantities like temperature in a turbulent fluid. Part 1. *J. Fluid Mech.* **5**, 113–133.

BROWNE, L. W. B. & ANTONIA, R. A. 1987 The effect of wire length on temperature statistics in a turbulent wake. *Exps. Fluids* **5**, 426–428.

BROWNE, L. W. B., ANTONIA, R. A. & SHAH, D. A. 1987 Turbulent energy dissipation in a wake. *J. Fluid Mech.* **179**, 307–326.

CHASNOV, J. R. 1996 Some similarity states of stably-stratified homogeneous turbulence. *Dyn. Atmos. Oceans* **23**, 183–192.

CORRSIN, S. 1952 Heat transfer in isotropic turbulence. *J. Appl. Phys.* **23**, 113–118.

FERNANDO, H. J. S. 1991 Turbulent mixing in stratified fluids. *Ann. Rev. Fluid Mech.* 455–493.

FINCHAM, A. M., MAXWORTHY, T. & SPEDDING, G. R. 1994 The horizontal and vertical structure of the vorticity field in freely-decaying, stratified grid turbulence. *Fourth Intl Symp. on Stratified Flows, Grenoble, France,* Vol. 2 (ed. E. Hopfinger, B. Voisin & G. Chavand).

GERZ, T. & SCHUMANN, U. 1991 Direct simulation of homogeneous turbulence and gravity waves in sheared and unsheared stratified flows. In *Turbulent Shear Flows 7*, Springer.

GIBSON, C. H. 1980 Fossil temperature, salinity, and vorticity turbulence in the ocean. In *Marine Turbulence*, pp. 221–257. Elsevier.

HAUGHDAL, J. & LIENHARD V, J. H. 1988 A low-cost, high-performance cold-wire bridge. *J. Phys.* E: *Sci. Instrum.* **21**, 167–170.

HERRING, J. R. & MÉTAIS, O. 1989 Numerical experiments in forced stably stratified turbulence. *J. Fluid Mech.* **202**, 97–115.

ITSWEIRE, E. C., HELLAND, K. N. & VAN ATTA, C. W. 1986 The evolution of grid-generated turbulence in a stably stratified fluid. *J. Fluid Mech.* **162**, 299–338.

ITSWEIRE, E. C., KOSEFF, J. R., BRIGGS, D. A. & FERZIGER, J. H. 1993 Turbulence in stratified shear flows: implications for interpreting shear-induced mixing in the ocean. *J. Phys. Oceanogr.* **23**, 1508–1522.

KOOP, C. G. & BROWAND, F. K. 1979 Instability and turbulence in a stratified fluid with shear. *J. Fluid Mech.* **93**, 135–159.

KRISHNAMOORTHY, L. V. & ANTONIA, R. A. 1987 Temperature-dissipation measurements in a turbulent boundary layer. *J. Fluid Mech.* **176**, 265–281.

LEBLOND, P. H. & MYSAK, L. A. 1978 *Waves in the Ocean.* Elsevier.

LIENHARD V, J. H. & VAN ATTA, C. W. 1989 Thermally stratifying a wind tunnel for buoyancy influenced flows. *Exps. Fluids.* **7**, 542–546.

LIENHARD V, J. H. & VAN ATTA, C. W. 1990 The decay of turbulence in thermally stratified flow. *J. Fluid Mech.* **210**, 57–112.

MILLS, R. R., KISTLER, A. L., O'BRIEN, V. & CORRSIN, S. 1958 Turbulence and temperature fluctuations behind a heated grid. *NACA Tech. Note* 4288.

OBUKHOV, A. M. 1954 Statistical description of continuous fields. *Trudy Geophys. Inst. Acad. Sci. USSR* No. 24(151).

PANCHEV, S. 1971 *Random Functions and Turbulence.* Pergamon.

SIRIVAT, A. & WARHAFT, Z. 1983 The effect of a passive cross-stream temperature gradient on the evolution of temperature variance and the heat flux in grid turbulence. *J. Fluid Mech.* **128**, 323–346.

STILLINGER, D. C., HELLAND, K. N. & VAN ATTA, C. W. 1983 Experiments on the transition of homogeneous turbulence to internal waves in a stratified fluid. *J. Fluid Mech.* **131**, 91–122.

TAYLOR, G. I. 1935 Statistical theory of turbulence, Part I. *Proc. R. Soc. Lond.* A **151**, 421–444.

THORODDSEN, S. T. & VAN ATTA, C. W. 1989 Anisotropy and dissipation in stably stratified grid turbulence. *Bull. Am. Phys. Soc.* **34**, 2321, Abstract only.

THORODDSEN, S. T. & VAN ATTA, C. W. 1992*a* The influence of stable stratification on small-scale anisotropy and dissipation in turbulence. *J. Geophys. Res.* **97**, C3, 3647–3658.

THORODDSEN, S. T. & VAN ATTA, C. W. 1992*b* Exponential tails and skewness of density-gradient probability density functions in stably stratified turbulence. *J. Fluid Mech.* **244**, 547–566.

TONG, C. N. & WARHAFT, Z. 1994 On passive scalar derivative statistics in grid turbulence. *Phys. Fluids* **6**, 2165–2176.

TURNER, J. S. 1973 *Buoyancy Effects in Fluids.* Cambridge University Press.

VAN ATTA, C. W. 1977 Second-order spectral local isotropy in turbulent scalar fields. *J. Fluid Mech.* **80**, 609–615.

VAN ATTA, C. W. 1985 Stratified-turbulence experiments. In *Turbulence and Predictability in Geophysical Fluid Dynamics and Climate Dynamics.* Corso Soc. Italiana di Fisica - Bologna - Italy.

VAN ATTA, C. W. 1991 Local isotropy of the smallest scales of turbulent scalar and velocity fields. *Proc. R. Soc. Lond.* A **434**, 139–147.

WARHAFT, Z. & LUMLEY, J. 1978 An experimental study of the decay of temperature fluctuations in grid-generated turbulence. *J. Fluid Mech.* **88**, 659–684.

YAP, C. & VAN ATTA, C. W. 1993 Experimental studies of the development of quasi-two-dimensional turbulence in stably stratified flow. *Dyn. Atmos. Ocean* **19**, 289–323.

YEH, T. T. & VAN ATTA, C. W. 1973 Spectral transfer of scalar and velocity fields in heated-grid turbulence. *J. Fluid Mech.* **58**, 233–261.

YOON, K. & WARHAFT, Z. 1990 The evolution of grid generated turbulence under conditions of stable thermal stratification. *J. Fluid Mech.* **215**, 601–638.